UC Berkeley
UC Berkeley Previously Published Works

Title

One-dimensional alignment of defects in a flexible metal-organic framework

Permalink

https://escholarship.org/uc/item/9rt9t87f

Journal

Science Advances, 9(6)

ISSN

2375-2548

Authors

Fu, Yao
Forse, Alexander C
Kang, Zhengzhong
et al.

Publication Date

2023-02-10

DOI

10.1126/sciadv.ade6975

Peer reviewed

CHEMISTRY

One-dimensional alignment of defects in a flexible metal-organic framework

Yao Fu[1,2,3], Alexander C. Forse[3,4,5], Zhengzhong Kang[2], Matthew J. Cliffe[6], Weicheng Cao[2], Jinglin Yin[2], Lina Gao[2], Zhenfeng Pang[2], Tian He[2], Qinlong Chen[2], Qi Wang[2], Jeffrey R. Long[3,5,7], Jeffrey A. Reimer[3], Xueqian Kong[1,2]*

Crystalline materials are often considered to have rigid periodic lattices, while soft materials are associated with flexibility and nonperiodicity. The continuous evolution of metal-organic frameworks (MOFs) has erased the boundaries between these two distinct conceptions. Flexibility, disorder, and defects have been found to be abundant in MOF materials with imperfect crystallinity, and their intricate interplay is poorly understood because of the limited strategies for characterizing disordered structures. Here, we apply advanced nuclear magnetic resonance spectroscopy to elucidate the mesoscale structures in a defective MOF with a semicrystalline lattice. We show that engineered defects can tune the degree of lattice flexibility by combining both ordered and disordered compartments. The one-dimensional alignment of correlated defects is the key for the reversible topological transition. The unique matrix is featured with both rigid framework of nanoporosity and flexible linkage of high swellability.

INTRODUCTION

Structural flexibility can bring unusual properties such as negative gas adsorption (*1, 2*), stimuli responsiveness (*3*), and stereochemical selectivity (*4, 5*) to porous materials. Metal-organic frameworks (MOFs), as an emerging class of porous materials, are endowed with tunable functionalities and diverse three-dimensional (3D) topologies (*6, 7*). Flexibility in MOFs (*8*) manifests as localized structural changes, e.g., linker rotation (*9*), or as correlated structural changes such as volume expansion and subunit displacement (*10–12*). In addition, the flexibility in MOFs is often associated with defects and disorder, showing the crossover characteristics of crystalline frameworks and soft materials (*13–16*). The integration of crystalline and disordered compartments as well as local and correlated structural dynamics has advanced into the frontiers of solid-state chemistry (*17–20*). However, the merits of defects and disorder in MOFs have long been underappreciated, largely because they are inaccessible by common characterization techniques. Different techniques and strategies are required to uncover the intricate interplay between flexibility, disorder, and defects in these hybrid solids.

In this work, we engineered a special type of defect and created a tunable degree of flexibility in the framework $Mg_2(dobpdc)$ ($dobpdc^{4-}$ = 4,4′-dioxido-3,3′-biphenyldicarboxylate) (*21–23*) by introducing nonbridging ligand modulators (fluorinated salicylic acid). This MOF represents a widely used structural analog of MOF-74 (*24, 25*) that adopts a honeycomb-like topology and features open metal sites. Defects in similar MOFs can lead to enhanced performance for adsorption or catalysis (*26–31*), yet the

critical information of defect structure and arrangement has not been revealed. The amorphization of MOF matrices with defects hampers structure determination by diffraction and microscopy techniques (*32–34*).

We hypothesized that a combination of advanced solid-state nuclear magnetic resonance (SSNMR) techniques (*35–40*) would be able to decode the arrangement of defects in partially amorphized $Mg_2(dobpdc)$. Spatially interconnected multispin interactions (e.g., ^{13}C-^{19}F and ^{19}F-^{19}F dipolar couplings) can map the location and distribution of defects beyond single unit cells and are sensitive to both local and correlated dynamic changes (*35, 41, 42*). The results of our experiments show that defective $Mg_2(dobpdc)$ frameworks undergo a reversible topological transition upon the removal or reintroduction of solvent. This flexible transition can be easily tuned by varying the stoichiometric ratio of defect-forming modulators. The semicrystalline lattice encompasses both permanent porosity for gas adsorption and high swellability in organic vapor, combining the merits of crystalline and noncrystalline materials. Assisted by molecular dynamics (MD) simulations, we show that the defects are aligned in a 1D fashion along the framework channel axis. Our study demonstrates an illustrative case of an MOF material wherein defects, disorder, and flexibility synergize, and the investigation provides understanding of hybrid structures on the mesoscale.

RESULTS AND DISCUSSION

Construction of defective $Mg_2(dobpdc)$

Defect-containing $Mg_2(dobpdc)$ samples were synthesized by adding varying amounts of 4-fluorosalicylic acid (H_2Fs) to the synthesis mixture (Fig. 1A). Because H_2Fs has only half of the coordination sites (hydroxyl and carboxylate groups) as the $H_4dobpdc$ [4,4′-dihydroxy-(1,1′-biphenyl)-3,3′-dicarboxylic acid] linker, we hypothesize that Fs^{2-} can partially substitute $dobpdc^{4-}$ linkers in the MOF to create substitutional defects. The defective samples are referred to as "*x*D," where *x* represents the concentration of

[1]Department of Physical Medicine and Rehabilitation, Sir Run Run Shaw Hospital, Zhejiang University, Hangzhou 310027, P. R. China. [2]Department of Chemistry, Zhejiang University, Hangzhou 310027, P. R. China. [3]Department of Chemical and Biomolecular Engineering, University of California, Berkeley, CA 94720, USA. [4]Department of Chemistry, University of Cambridge, Cambridge CB2 1EW, UK. [5]Department of Chemistry, University of California, Berkeley, CA 94720, USA. [6]School of Chemistry, University of Nottingham, University Park, Nottingham NG7 2RD, UK. [7]Materials Sciences Division, Lawrence Berkeley National Laboratory, Berkeley, CA 94720, USA.
*Corresponding author. Email: kxq@zju.edu.cn
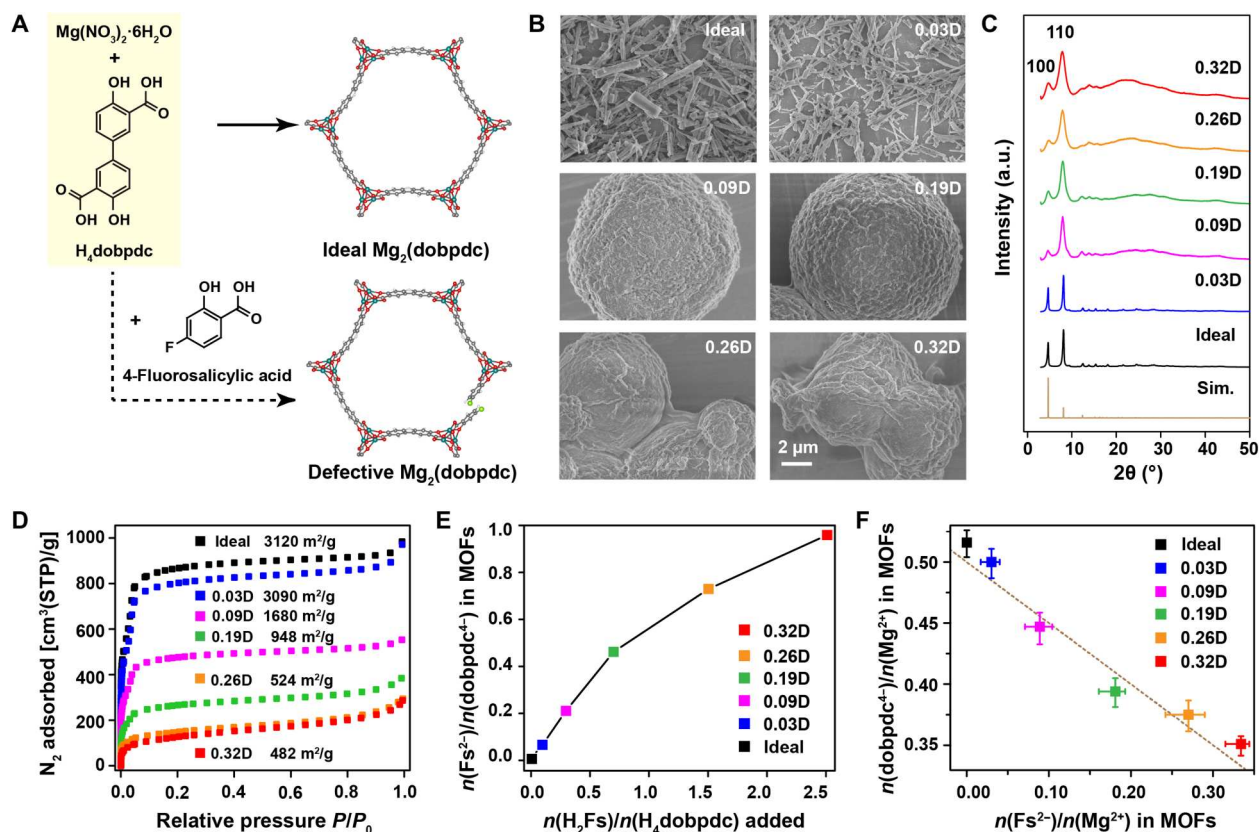
Fig. 1. General characterizations of Mg$_2$(dobpdc). (**A**) Schematic illustrations of the preparations for ideal and defective Mg$_2$(dobpdc). (**B**) SEM images of Mg$_2$(dobpdc) samples with various defect concentrations. Scale bar, 2 μm (for all images). (**C**) PXRD patterns obtained on as-synthesized Mg$_2$(dobpdc) samples. a.u., arbitrary units. (**D**) N$_2$ adsorption isotherms measured at 77 K for samples activated under vacuum at 250°C. The BET surface areas are shown. (**E**) Molar ratios of coordinated Fs^{2-} to dobpdc^{4-} (measured by solution-state ^{1}H NMR of digested samples) plotted against the molar ratios of added H$_2$Fs to H$_4$dobpdc during synthesis. (**F**) Molar ratios of dobpdc^{4-} to Mg^{2+} [n(dobpdc^{4-})/n(Mg^{2+})] plotted against the molar ratios of Fs^{2-} to Mg^{2+} [n(Fs^{2-})/n(Mg^{2+})] in the MOF samples. The dotted line indicates the charge balance. The horizontal and vertical error bars come from the standard deviations (SDs) of the inductively coupled plasma optical emission spectrometry and NMR measurements.

defects in the MOF. An ideal Mg$_2$(dobpdc) sample (referred to as "ideal") was also prepared for comparison. The detailed synthetic procedures are provided in the Supplementary Materials. Scanning electron microscopy (SEM) images (Fig. 1B) show that, with a low concentration of defects (0.03D), the particles form as elongated rods similar to that of the ideal sample. However, for samples with more defects, the particles grow into large sphere-like or irregular shapes with a distribution of diameters from 3 to 15 μm (fig. S1). These large particles are polycrystalline aggregates of smaller crystallites.

Figure 1C presents the powder x-ray diffraction (PXRD) patterns of as-synthesized MOF samples (with methanol solvent remaining in the pores). As the samples become more defective, the peaks broaden markedly, yet the lattice dimensions are maintained even with a high density of defects. Fitting of the PXRD patterns shows that the lattice parameter a expands by ~1% for as-synthesized defective MOFs (fig. S2). In addition, the peak broadening suggests reduced crystallinity in defective samples, which corresponds to the decrease of Scherrer size from 65 nm (0.03D) to 6 nm (0.32D) upon increasing defect concentration (fig. S2). The apparent reduction of the {100} diffraction peak in most defective samples can be attributed to the packing disorder of Fs^{2-} ligands (fig. S3).

The specific Brunauer-Emmett-Teller (BET) surface area of each material is determined from N$_2$ adsorption data collected at 77 K on samples activated at 250°C (with methanol removed). The BET surface area of defective Mg$_2$(dobpdc) decreases from above 3000 m^2/g [as high as that of the ideal sample (43)] to ~500 m^2/g as the defect concentration increases (Fig. 1D). Thermogravimetric analysis (TGA) shows that the series of defective Mg$_2$(dobpdc) can withstand up to 400°C in nitrogen flow without notable degradation, suggesting that they are as thermally stable as the ideal sample (fig. S4).

The chemical composition of each defective Mg$_2$(dobpdc) sample is studied by solution-state ^{1}H NMR spectroscopy (fig. S5 and table S2) and inductively coupled plasma optical emission spectrometry (ICP-OES) (table S3) on the acid-digested samples. The results (Fig. 1E) show that, by increasing the relative concentration of H$_2$Fs during synthesis, the quantity of incorporated Fs^{2-} can reach almost a 1:1 ratio with respect to the dobpdc^{4-} linker (as in 0.32D). Adding extra H$_2$Fs did not result in appropriate products under the same synthetic condition. To understand the stoichiometry in defective Mg$_2$(dobpdc), we plot the molar ratios of (dobpdc)$^{4-}$ to Mg^{2+} [i.e., n(dobpdc^{4-})/n(Mg^{2+})] against the molar ratios of Fs^{2-} to Mg^{2+} [i.e., n(Fs^{2-})/n(Mg^{2+})] (Fig. 1F). The

analysis shows that the charge balance in defective $Mg_2(dobpdc)$ compounds is maintained: $(+2) \times n(Mg^{2+}) + (-4) \times n(dobpdc^{4-}) + (-2) \times n(Fs^{2-}) = 0$ (marked as the dotted line in Fig. 1F). Therefore, the overall formula for defective $Mg_2(dobpdc)$ can be written as $Mg_2(dobpdc)_{1-x}(Fs)_{2x}$, where x represents the concentration of defects. The removal of x $dobpdc^{4-}$ linkers is compensated by $2x$ Fs^{2-} modulators, which supports a charge of $2-$ for the incorporated Fs^{2-} species instead of a protonated form. These findings also support the hypothesis that Fs^{2-} molecules serve as substitutional defects in defective $Mg_2(dobpdc)$ materials.

Reversible order-to-disorder transition

The structural flexibility of defective $Mg_2(dobpdc)$ can be observed on multiple scales using various techniques. The SEM morphology and spectroscopic features of defective $Mg_2(dobpdc)$ (taking 0.32D as an example) undergo marked changes when the sample is with or without solvent (methanol). As illustrated in Fig. 2A, the as-synthesized sample, which holds residual methanol in its pores, is referred to here as "wet"; the sample dried at room temperature under vacuum, in which the weakly adsorbed methanol was eliminated,

is referred to as "dry"; and the dried sample resoaked with methanol (overnight) is referred to as "rewet." Note that the conditions for preparing the dry sample are relatively mild (vacuum at room temperature), which should remove weakly adsorbed methanol, yet methanol coordinated to the open metal sites should remain. When weakly adsorbed methanol is removed from the pores, the relatively large aggregated particles (~5 μm) in the wet sample scatter and contract into smaller pieces (~500 nm) in the dry sample. However, the small pieces swell and reassemble into large particles when the dry sample is resoaked with methanol (Fig. 2B). The morphological transition indicates that the framework of defective $Mg_2(dobpdc)$ is highly swellable. Defective $Mg_2(dobpdc)$ can uptake 10 times as much methanol vapor as compared to the ideal sample (fig. S6). We attribute the strong swellability to a better surface wettability of defective MOF particles and more efficient intraparticle diffusion of methanol. The ability to strongly adsorb organic volatiles could be useful for air pollutant removal (44) or adsorption heat pumps (45).

In terms of the PXRD patterns (Fig. 2C and figs. S2 and S7), the persistence of the strong {110} peak, which corresponds to the
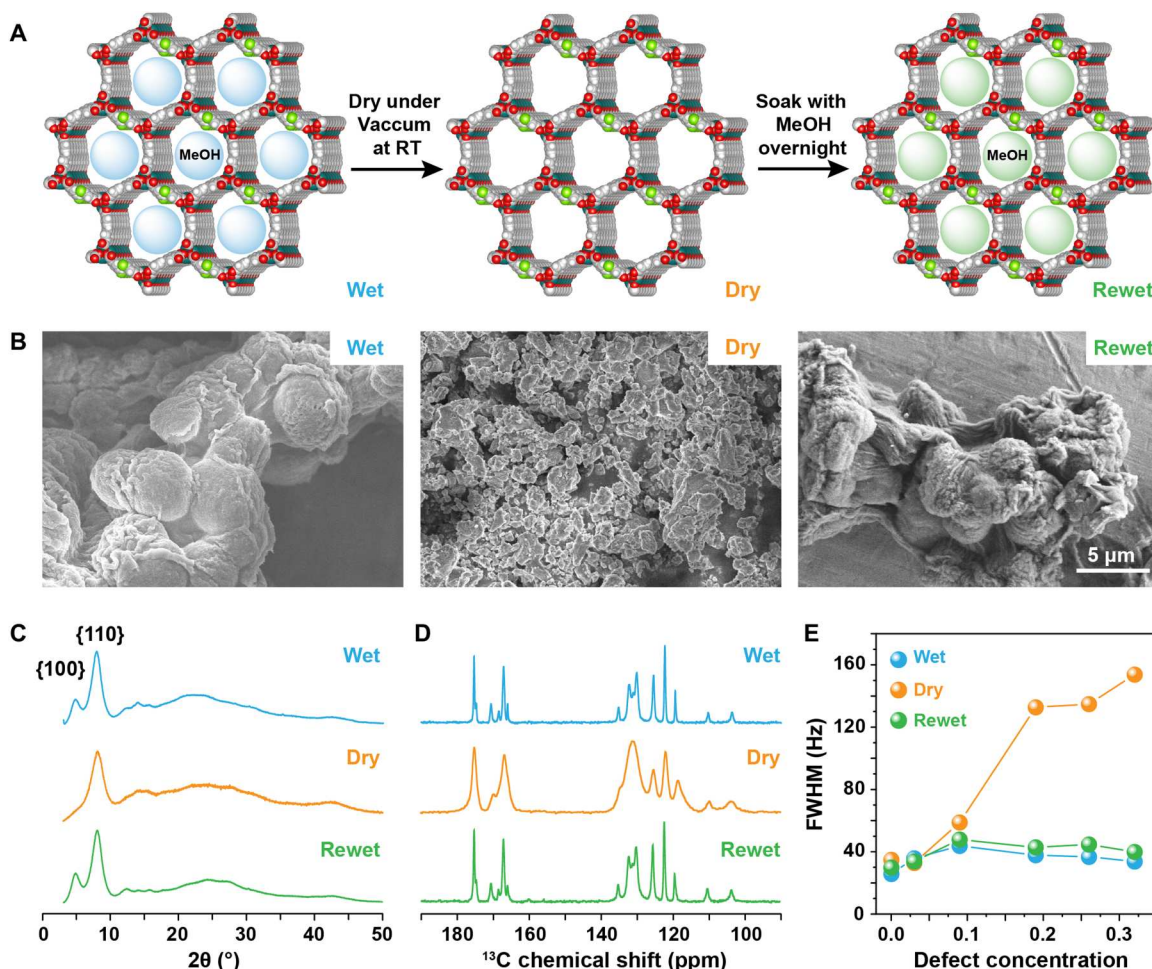
Fig. 2. The dynamic structural changes of defective Mg₂(dobpdc). (**A**) Illustrations of solvent (i.e., methanol) removal and reintroduction in $Mg_2(dobpdc)$. Characterizations of the "wet," "dry," and "rewet" samples (0.32D). (**B**) SEM images. Scale bar, 5 μm (for all images). (**C**) PXRD patterns and (**D**) ^{13}C cross-polarization–magic angle spinning spectra of the defective $Mg_2(dobpdc)$ under different conditions. (**E**) Full width at half maximum (FWHM) of ^{13}C peak at 122-ppm plotted against the defect concentration. The FWHM can be regarded as the representation of "degree of disorder" for local chemical bonds in the MOF samples.

nearest linker-linker distance, suggests that the honeycomb lattice of $Mg_2(dobpdc)$ retains. Meanwhile, the decrease of intensity of the {100} peak could be attributed to the loss of solvent in the dry samples. The large widths of the peaks make precise determination of lattice parameters via a Pawley refinement of the PXRD patterns challenging, particularly for the c parameter (fig. S2B). However, the a parameter contracts by ~1% upon drying the defective samples, as might be expected for the loss of the honeycomb ordering (fig. S2A).

PXRD data primarily characterize the compartments with long-range order yet provide limited information on the noncrystalline compartments. SSNMR can supplement PXRD to offer a more holistic picture of these semicrystalline materials. For instance, the full width at half maximum (FWHM) of ^{13}C cross-polarization (CP)–magic angle spinning (CPMAS) signals (Fig. 2D) shows apparent differences between the dry and wet samples. The FWHM corresponds to the degree of disorder of local chemical bonds, including primarily variations in the bond lengths and torsion angles. Here, the effects of motion-induced T_2 relaxation can be neglected as it only contributes a minor faction of FWHM (fig. S8). The measurement (Fig. 2E and fig. S8) shows that the dry samples generally have a higher degree of disorder than the corresponding wet or rewet samples [the 122–parts per million (ppm) peak of the $dobpdc^{4-}$ linker is used as representative]. The local disorder of the framework gradually increases as more defects are introduced. Moreover, the degree of order is about the same for both wet and rewet samples, indicating a reversible order-to-disorder transition. The PXRD and SSNMR characterizations (figs. S7 to S9) on the series of samples demonstrate that the flexibility of both long-range and local ordering can be tuned continuously by varying the concentration of defects. In addition, we show that the order-to-disorder transition is reversible even after three cycles of drying and resoaking procedure (fig. S10).

The structure and geometric alignment of defects

It is intriguing that $Mg_2(dobpdc)$ can accommodate such a high density of defects while maintaining the honeycomb topology. The coordination structure of the Fs^{2-} ligands is important for understanding the defect formation in the framework. On the basis of the variable contact time ^{13}C CPMAS experiments (fig. S11) and assisted with $^{13}C\{^{19}F\}$ rotation-echo double resonance (REDOR) (figs. S12 and S13), we distinguish the ^{13}C NMR signals that belong to the Fs^{2-} ligand and $dobpdc^{4-}$ linker individually. The assignments of characteristic ^{13}C peaks are shown in fig. S11. The apparent shift of resonance positions in Fs^{2-} ligand from those in the H_2Fs precursor is consistent with the deprotonation of the carboxylate and hydroxyl groups.

The REDOR experiment is a powerful technique for accurately determining internuclear distances in simple spin systems (41, 46). It measures the spin-spin dipolar interaction (for ^{13}C and ^{19}F here), which correlates with the ^{13}C-^{19}F distance (when the spins are rigid). The experiments render decay curves of relative intensity (S/S_0) of ^{13}C signal under variable periods of ^{19}F irradiation (Fig. 3A). The $^{13}C\{^{19}F\}$ REDOR curves that correspond to intramolecular ^{13}C-^{19}F interactions within Fs^{2-} linkers (Fig. 3B and fig. S13) agree with the expected intramolecular distances analytically. The agreeable results and multiple variable-temperature experiments (fig. S14) indicate that motional interference is absent on the time scale of our NMR measurements.

We further investigated the intermolecular ^{13}C-^{19}F interactions for ^{13}C spins on $dobpdc^{4-}$ linkers and ^{19}F spins on Fs^{2-} ligands. Because of the heterogeneous spatial arrangements of linkers and defects in defective $Mg_2(dobpdc)$, the intermolecular ^{13}C-^{19}F interaction reflects the highly complex multispin system. For a simplified treatment, we can derive the average distances between $dobpdc^{4-}$ and Fs^{2-} at the specified positions (see Fig. 3A). We find that the average intermolecular separation decreases to ~6 to 7 Å in the dry 0.32D sample as compared to ~10 Å in the wet or ~9 Å in the rewet sample (Fig. 3C). This decrease is likely due to the partial shrinkage of pore volume in the dry sample. The almost complete restoration of intermolecular distance in the rewet sample also supports the reversible transition, as described in the previous section. Consistent results are observed for other ^{13}C-^{19}F spin pairs and in the sample with a lower density of defects (fig. S14).

To further understand the spatial arrangement of the Fs^{2-} ligands, we take advantage of the intermolecular ^{19}F-^{19}F spin-spin interactions that are contributed to by fluorine atoms on the Fs^{2-} ligands. The ^{19}F-^{19}F interaction can be probed by a ^{19}F center-band-only detection of exchange (CODEX) experiment, which examines the propagation of through-space spin diffusion process (involving both ^{19}F and ^{1}H spins) (47, 48). Notably, the dominant ^{19}F signal at −108 ppm (92% molar fraction) of the wet 0.32D sample is affected by the CODEX measurement, while the minor signal at −105 ppm (8% molar fraction) is not, suggesting that only a minor proportion of the Fs^{2-} ligands are isolated and have no Fs^{2-} neighbors (Fig. 3D and fig. S15).

CODEX measurements provide a relative intensity (S/S_0) of the ^{19}F signal under variable mixing periods of spin diffusion (Fig. 3E). The curves not only correlate to the ^{19}F-^{19}F separations but also can be modeled to infer the spatial distribution of a collection of spins (42). In the defective $Mg_2(dobpdc)$, we consider four possible geometries of spatial arrangements of Fs^{2-} ligands: 3D, 2D, and 1D arrangements with a uniform spacing (1D uniform) and with nonuniform spacings (1D nonuniform), as illustrated in fig. S16. The numerical model (47) shows that the experimental ^{19}F CODEX curve is best matched by the 1D nonuniform geometry and is incompatible with other geometries (Fig. 3E and fig. S17). This result is consistent with the model of defective $Mg_2(dobpdc)$ optimized by MD simulations in which the Fs^{2-} ligands are aligned along the c axis of the lattice, and the separations between ^{19}F spins are 3.2 and 6.5 Å (Fig. 3F). The alignment of Fs^{2-} ligands in defective $Mg_2(dobpdc)$ is also evidenced either in samples with various defect concentrations or in samples prepared under different treatment conditions (wet, dry, or rewet) (figs. S18 and S19). Nevertheless, the ^{19}F CODEX experiment alone cannot offer accurate determination of intermolecular distances because the CODEX decay also depends on the proton spin diffusion efficiency (47), which could be largely affected by the density and mobility of solvent molecules. Additional analyses are needed to decipher the topological arrangement of defects and their structural transitions.

The topological distribution of defects

$^{13}C\{^{19}F\}$ REDOR measurements have the high sensitivity and accuracy to quantify ^{13}C-^{19}F distances, and the results can be used as a quantitative determinant of spatial arrangement (41). Therefore, we attempt to further validate the proposed 1D alignment of defects
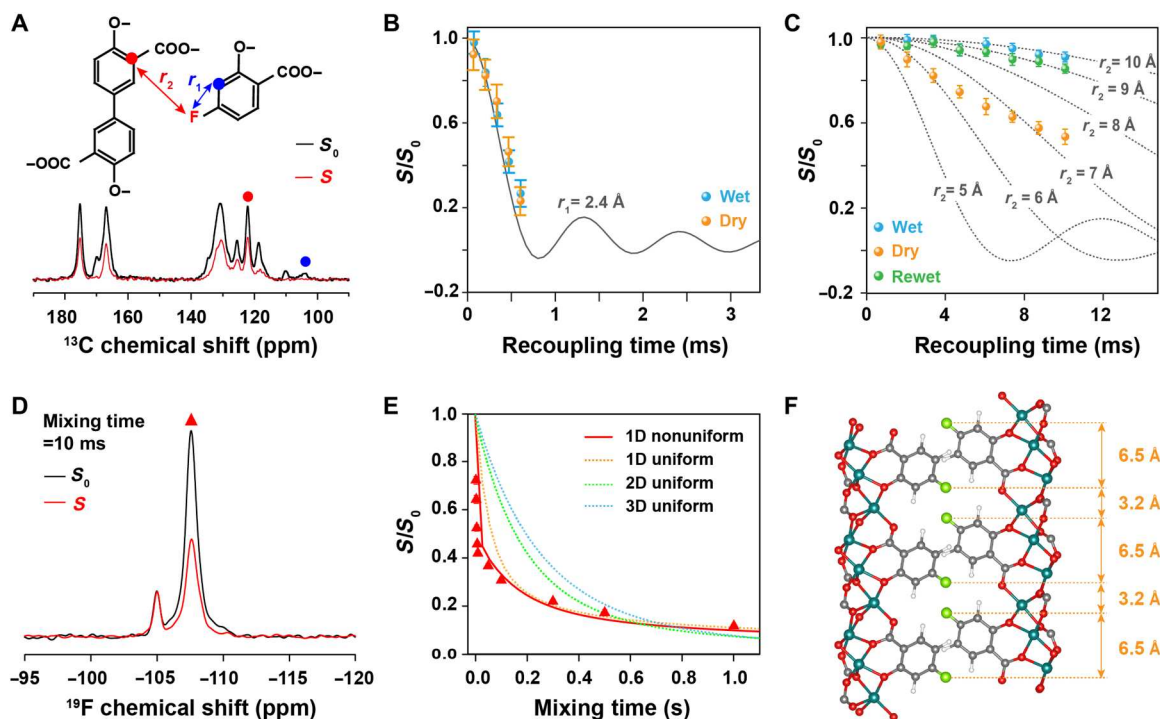
Fig. 3. Measurements of intermolecular separations. (**A**) Top: Schematic illustration of intramolecular distance (r_1) between ^{13}C spins (marked as the blue rot) and ^{19}F spins on the Fs^{2-} ligand and intermolecular distance (r_2) between the ^{13}C spins (marked as the red rot) on dobpdc^{4-} linker and ^{19}F spins on the Fs^{2-} ligand, both measured by the REDOR experiments. Bottom: Representative ^{13}C spectra obtained in ^{13}C{^{19}F} REDOR experiments. Spectrum S_0 represents the ^{13}C spectrum taken without ^{19}F dipolar modulation, and S is the ^{13}C spectrum with ^{19}F dipolar modulation. (**B**) ^{13}C{^{19}F} REDOR decay curve for the intramolecular ^{13}C-^{19}F spin pair on the Fs^{2-} ligand. The experimental data agree with the theoretical REDOR decay for a ^{13}C-^{19}F spin pair with a distance of r_1 = 2.4 Å (the solid black line). (**C**) ^{13}C{^{19}F} REDOR decay curves for the intermolecular ^{13}C-^{19}F couplings between the dobpdc^{4-} linker and the Fs^{2-} ligand in 0.32D sample measured at 300 K. The dotted lines are theoretical REDOR curves for isolated ^{13}C-^{19}F spin pairs of internuclear distance r_2. The error bars are the SDs propagated from the signal-to-noise ratios of NMR spectra. (**D**) Representative ^{19}F reference signal (S_0) and decay signal (S) measured with a ^{19}F centerband-only detection of exchange (CODEX) experiment. (**E**) ^{19}F CODEX S/S_0 decay of the −108-ppm peak for the wet 0.32D sample measured at 300 K. The solid and dotted lines are simulation results based on different spatial distributions as shown in fig. S16. (**F**) Structure depicting the directional alignment of Fs^{2-} ligands in parallel with the *c* axis in defective Mg$_2$(dobpdc). Blue, red, gray, white, and green spheres represent Mg, O, C, H, and F atoms, respectively.

using ^{13}C{^{19}F} REDOR experiments. To do this, we construct a library of comprehensive defect models (fig. S20), all of which are refined by MD simulations, and then analyzed against features of the calculated REDOR curves. The hypothetical models take the known concentration of Fs^{2-} ligands [i.e., n(Fs^{2-}):n(dobpdc^{4-}) = ~1:1 in the 0.32D sample] and consider the possible distributions in an extended super lattice. The initial models are filled with methanol solvent to represent the wet state.

In general, these models can be categorized into three scenarios: a completely random distribution of defects in the 3D lattice (Fig. 4A, top), 2D extended defects in the *ab* plane interlayered randomly between nondefect planes (Fig. 4A, middle), and 1D stacked defects aligned along the *c* axis (Fig. 4A, bottom). On the basis of these scenarios, the distributions of intermolecular ^{13}C-^{19}F distances can be obtained (Fig. 4B). The hypothetical ^{13}C{^{19}F} REDOR curves corresponding to the ^{13}C-^{19}F distance distributions are plotted in Fig. 4C. Here, the multispin dipolar couplings between a ^{13}C with multiple ^{19}F are considered in the simulation (49). Because a number of possible models have been analyzed, the REDOR curves are shown collectively as spread bands instead of as individual lines. The spread of REDOR curves for the 3D random distribution is relatively broad because there are a greater

number of possibilities, while the spread for the 2D planar and 1D aligned distributions is relatively narrow.

In a further crucial step, we consider the structural transition from the wet state to the dry state. The dry models are obtained through MD optimizations of the structures without physically adsorbed methanol. As we expect, the local coordination structure for the Fs^{2-} ligands becomes more disordered in the dry state (as shown in the schematic illustrations in figs. S21 to S24). However, the most notable feature appears in the 1D aligned scenario in which partial lattice is markedly distorted (figs. S23 and S24), and this leads to a pronounced difference between the wet and dry samples for their ^{13}C-^{19}F distance distributions (Fig. 4B). In contrast, the lattices for the 3D random and 2D planar scenarios are not substantially affected by solvent removal (figs. S21 and 22).

By comparing the REDOR curves of both the wet and dry states between hypothetical models and the experimental data (Fig. 4C), we conclude that a 1D aligned topology is the most probable scenario for defective Mg$_2$(dobpdc). This alignment of the Fs^{2-} ligands is also supported by density functional theory (DFT) calculations which show that aligned Fs^{2-} ligands along *c* axis are more energetically stable than neighboring arrangement in the *ab* plane (fig. S25). The deviations of the experimental REDOR curves from the
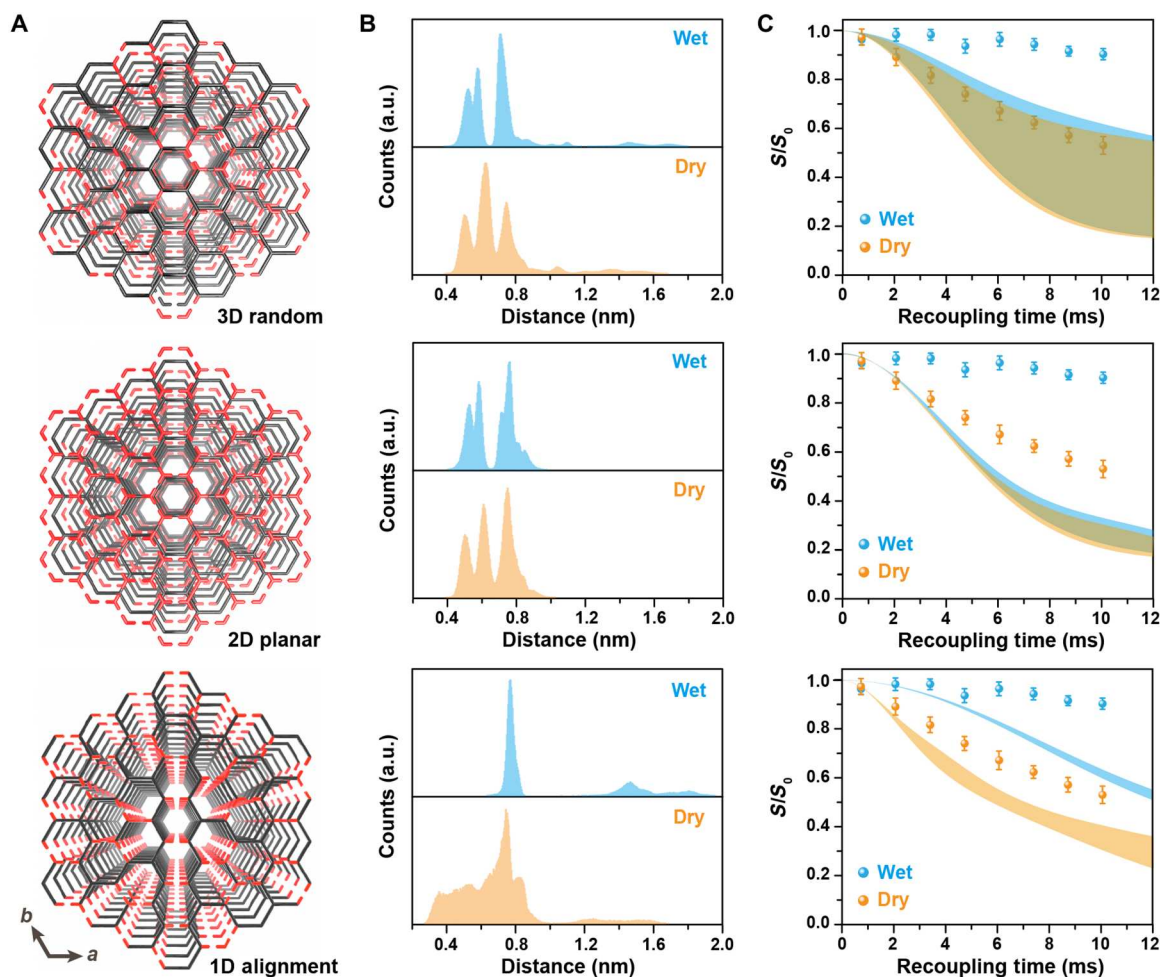
Fig. 4. Determining the topological distribution of defects. (**A**) Hypothetical defect distributions in defective $Mg_2(dobpdc)$: (top) 3D random distribution, (middle) 2D planar distribution in layers, and (bottom) 1D alignment in parallel with the *c* axis. The Fs^{2-} ligands are shown as dashed red lines, and $dobpdc^{4-}$ linkers are shown as black lines. (**B**) Statistical distribution of distances between the selected carbon atoms of $dobpdc^{4-}$ (at 122 ppm) and the nearest F atoms of Fs^{2-}. The results are obtained from the corresponding structural motifs that are optimized by MD simulations for both wet and dry conditions. (**C**) Calculated $^{13}C\{^{19}F\}$ REDOR curves based on the ^{13}C-^{19}F distance distributions for different scenarios. As each scenario corresponds to a number of possible motifs, the REDOR curves are shown as colored bands (blue for wet and orange for dry) to show the spread of ranges. Experimental REDOR data points are shown as colored spheres. The error bars are the SDs propagated from the signal-to-noise ratios of NMR spectra.

1D aligned models (Fig. 4C, bottom) could arise from the small fraction of isolated Fs^{2-} ligands and/or from the simplified structural motifs.

The unique 1D alignment of correlated defects endows the lattice with topological flexibility as it allows the dislocation of different compartments. This topological flexibility leads to the high swellability of defective $Mg_2(dobpdc)$ in methanol vapor. Meanwhile, the aligned defects coexist with intact crystalline compartments, which provide available porosity for gas adsorption, unlike many amorphous MOFs that are depleted of porosity (*50*, *51*).

In summary, we have successfully engineered an MOF matrix by introducing tunable ratios of defects. This defective matrix encompasses both rigid crystalline compartments and flexible noncrystalline compartments. Our study not only uncovers the unusual 1D alignment of defects but also offers an understanding of the both short-range and long-range transitions in the semicrystalline framework. The combined SSNMR strategy for unveiling linker defect

distributions is indispensable for studying complex hybrid structures with or without long-range ordering.

MATERIALS AND METHODS
Materials
The compound $H_4dobpdc$ was obtained from Trylead Chemical Technology Co. Ltd. All other reagents and solvents were obtained from Sigma-Aldrich at reagent grade purity or higher and were used without further purification.

The defective $Mg_2(dobpdc)$ and ideal $Mg_2(dobpdc)$ were synthesized by the same method, albeit with different amounts of 4-fluorosalicylic acid (see table S1). The ligand $H_4dobpdc$ (0.411 g, 1.5 mmol), $Mg(NO_3)_2 \cdot 6H_2O$ (1.15 g, 4.5 mmol), and 4-fluorosalicylic acid (quantities given in table S1) were dissolved in 30 ml of a 55:45 (v/v) methanol:*N*,*N*-dimethylformamide (DMF) solution using sonication. Once all reagents were dissolved, the synthesis

mixtures were transferred to a 50-ml Teflon liner. The liners were sealed in stainless steel autoclaves, which were subsequently placed in an oven preheated to 120°C for 24 hours. The crude white powder precipitates were isolated by filtration and were then soaked in 50 ml of DMF for 12 hours at 120°C for three times, followed by solvent exchange by soaking in 50 ml of methanol for 12 hours at 60°C for three times. The methanol-solvated frameworks were collected by filtration and labeled as wet samples. Then, the wet samples were dried under vacuum for a minimum of 3 hours at room temperature to remove the free methanol and yielded dry samples. The dry powders were resoaked with methanol solvent overnight and then collected by filtration to obtain the rewet samples.

Methods

To analyze the loading of Fs^{2-} ligand, ~5 mg of each defective $Mg_2(dobpdc)$ powder was digested in a solution of 0.4 ml of 35 weight % (wt %) DCl in D_2O and 1 ml of dimethyl sulfoxide (DMSO)–d6 containing a known concentration of 1,3,5-trimethoxybenzene (as the internal standard for quantitation). The solution was sonicated and/or heated at 60°C until the solid fully dissolved. ^1H NMR spectra were acquired on Bruker AV-300, ABV-400, or AVQ-400 instruments at the University of California, Berkeley's NMR facility. The actual Fs^{2-} and $dobpdc^{4-}$ concentrations in MOF samples were determined from the ^1H signals of Fs^{2-} and $dobpdc^{4-}$ relative to that of the internal standard. The recycle delays for ^1H experiments were 2 s.

PXRD measurements were carried out on samples placed on a quartz holder using a Rigaku Ultimate-IV x-ray diffractometer operated at 40 kV/30 mA with Cu Kα line (λ = 1.5418 Å). Patterns were collected in reflectance Bragg-Brentano geometry in the 2θ range from 3° to 50°. The morphologies of MOF samples were observed on a field-emission SEM (FE-SEM) (Hitachi SU8000 FE-SEM) at 5 kV.

Nitrogen sorption measurements were performed at 77 K on BELSORP-max instrument. Before adsorption measurements, the $Mg_2(dobpdc)$ samples were pretreated (activated) under vacuum for 24 hours at 250°C. BET surface areas were calculated by fitting the isotherm data in the P/P_0 range of 0 to 0.1.

TGAs were conducted using a TA Instruments TGA Q5000 with a flow rate of 25 ml/min for N_2 gas. Thermogravimetric decomposition traces were collected under 100% N_2 with a temperature ramp rate of 1.5°C/min (fig. S2).

ICP-OES analysis was conducted on an ICP Optima 7000 DV instrument. MOF (~10 mg of) was sonicated and fully digested in 0.4 ml of 35 wt % HCl solution and 1 ml of DMSO. Fifty microliters of dissolved MOF solutions was diluted with 10 ml of pure H_2O. The diluted solutions were used to test the magnesium contents by ICP-OES. The Mg^{2+} concentration (milligram per liter) in different MOF samples was experimentally determined by referring to a magnesium standard curve made by $Mg(NO_3)_2$ solution.

Solid-state NMR Experiments

Solid-state NMR experiments were performed on a Bruker Avance 400 III HD spectrometer (magnetic field strength of 9.4 T) operating at resonance frequencies of 400.13 MHz for ^1H, 376.8 MHz for ^{19}F, and 100.61 MHz for ^{13}C using an HFXY magic angle spinning probe equipped with a 3.2-mm spinner module. The spinning speed was 15 kHz for all the experiments. The ^{13}C signals were referenced to the methylene signal of adamantane at 38.5 ppm, and ^{19}F signals

were referenced to that of ammonium trifluoroacetate at −72.0 ppm. The acquisition time for ^{13}C experiments was 40 ms, and the acquisition time for ^{19}F experiments was 10 ms. The spectral window for ^{13}C was 40 kHz, and the spectral window for ^{19}F was 150 kHz. Gaussian broadening was applied to obtain the optimum representations of NMR spectra.

For the ^{13}C CP spectra, the ramped CP sequence was applied and the ^{13}C signal was acquired under SPINAL-64 ^1H decoupling (100-kHz ^1H radiofrequency field). The contact times of 50 or 4000 μs was used for ^1H-^{13}C polarization transfer. The CP spin-lock field for ^{13}C was about 80 kHz, and the power on ^1H was ramped from 50 to 100 kHz. The recycle delays for ^{19}F experiments were 10 s to ensure the full return of the ^{19}F magnetization to equilibrium. For ^{13}C direct polarization experiments, the recycle delay was set to 120 s. Pulse lengths were 2.5 μs for ^1H 90° pulse, 2.4 μs for ^{19}F 90° pulse, and 3.0 μs for ^{13}C 90° pulse.

For $^{13}C\{^{19}F\}$ REDOR (46) experiments, the standard pulse sequence with ^{13}C detection and ^{19}F recoupling pulses was used (drawn in fig. S26). The REDOR experiments with (S) and without (S_0) 180° pulses on the ^{19}F channel were acquired for different recoupling times. The ratio of signal intensities (S/S_0) for different recoupling times gives a REDOR curve.

The pulse sequence for ^{19}F CODEX (48) experiment is shown in fig. S27. Two experiments, an exchange experiment (S) with variable spin diffusion mixing time t_m and a short z-filter time ($t_z = 1$ ms) as well as a reference experiment (S_0) with interchanged t_m and t_z, were acquired. The ratio of intensities, S/S_0, was measured as a function of the mixing time.

Computational methods

Structural motifs of defective Mg2(dobpdc)

The structural motifs of defective $Mg_2(dobpdc)$ are depicted by stacked hexagons (fig. S20). A black edge represents a single $dobpdc^{4-}$ linker, and a red edge represents two Fs^{2-} ligands. Hypothetical defect distributions in defective MOF 0.32D are shown in fig. S20. The distribution motifs are named as XYZ_n or XY_n, where X, Y, or Z represent the number of red edges in each hexagonal layer and the subscript n represents different scenarios. For building a hybrid superlattice of 1D aligned defects, we combined 222_2, 222_3, and 222_4 motifs.

MD simulations

Structures of ideal and defective $Mg_2(dobpdc)$ with incorporated methanol were optimized by DFT calculations at the level of B3LYP functional. The basis set of 6-31G* was used for C, H, O, and Mg atoms. These calculations were performed by Gaussian 09 package (52). The parameters of methanol and the defective $Mg_2(dobpdc)$ used in MD simulations were obtained in general AMBER force field form by the Antechamber tool (53). The restrained electrostatic potential (RESP) method was applied to determine the charge of MOFs and methanol molecules (54).

MD simulations were performed in the NPT ensemble in GROMACS package (55–57) (version 5.0.4). For the wet condition, the MOF matrices were fulfilled with methanol through PACKMOL package (58). For the dry condition, the free methanol molecules were removed and the coordinated methanol molecules were retained. Each simulation was performed for 50 ns with a time step of 2 fs. Data are saved every 4 ps. Periodic boundary conditions were applied in all simulations. The Nose-Hoover thermostat coupling method was used to maintain the temperature at 300 K (59).

The bond length was constrained by linear constraint solver algorithm in the simulations ([60]). For nonbonded van der Waals interaction, the cutoff switching function started at 1.2 nm and reached zero at 1.35 nm. For long-range electrostatic interaction calculated by the particle mesh Ewald summation method ([61]), the cutoff distance was set at 1.2 nm. The distance distribution analysis of ^{13}C-^{19}F atoms and the REDOR calculations were obtained from the last 1 ns of MD simulation. The VMD software was used to visualize simulation results ([62]).

The REDOR calculations considered the multispin effect ([49]) by introducing the average distance, $\langle r \rangle$, which satisfies the following relation

$$\frac{1}{\langle r \rangle^6} = \sum_{i=1}^{n} \frac{1}{r_i^6}$$

where r_i is the internuclear distances between a specified ^{13}C spin and all surrounding ^{19}F spins.

DFT energy calculations

Energy difference, $\Delta\Delta E$, between defective Mg_2(dobpdc) and ideal Mg_2(dobpdc) was calculated by the formula below

$$\Delta\Delta E = (E_{total,defect} - E_{total,ideal}) - (E_{Fs^{2-}} - E_{dobpdc^{4-}})$$

Here, $E_{total,\ defect}$ is the absolute energy of the defective MOF, $E_{total,\ ideal}$ is the absolute energy of the ideal MOFs, $E_{Fs^{2-}}$ is the absolute energy for the Fs^{2-} ligands in defective MOFs, and $E_{dobpdc^{4-}}$ is the absolute energy of the dobpdc^{4-} linkers in ideal MOFs. The absolute energy is calculated by DFT calculations at the level of B3LYP functional with basis 6-31G* basis set in Gaussian 09 package.

PXRD analysis

Pawley refinement of the powder diffraction data was carried using TOPAS-Academic 4.1 ([63], [64]). We first refined the data for the ideal wet sample, allowing the lattice parameters and peak shape to vary freely. For all other samples, the lattice parameters were freely refined, but the peak shape was modeled using the peak shape of the ideal wet sample and an additional Gaussian size broadening term. From this Gaussian size broadening, an effective crystallite size was determined. For all structures, the space group of ideal material was used (P3$_1$21).

The first two Bragg peaks, {100} and {110}, were modeled using a pseudo-Voigt peak shape, where peak position, area, and Lorentzian contribution were allowed to vary freely for each peak. The background was fitted using two-term Chebyshev polynomial (i.e., a linear and a constant term). An additional exponential convolution was applied (simple axial model) to account for instrumental peak asymmetry. From these refinements, we determined the relative peak intensities of the first two Bragg peaks.

Supplementary Materials

This PDF file includes:
Figs. S1 to S27
Table S1 to S3
References

REFERENCES AND NOTES

1. S. Krause, V. Bon, I. Senkovska, U. Stoeck, D. Wallacher, D. M. Többens, S. Zander, R. S. Pillai, G. Maurin, F. X. Coudert, S. Kaskel, A pressure-amplifying framework material with negative gas adsorption transitions. *Nature.* **532**, 348–352 (2016).

2. S. Krause, J. D. Evans, V. Bon, I. Senkovska, S. Ehrling, P. Iacomi, D. M. Többens, D. Wallacher, M. S. Weiss, B. Zheng, P. G. Yot, G. Maurin, P. L. Llewellyn, F.-X. Coudert, S. Kaskel, Engineering micromechanics of soft porous crystals for negative gas adsorption. *Chem. Sci.* **11**, 9468–9479 (2020).

3. R. Pallach, J. Keupp, K. Terlinden, L. Frentzel-Beyme, M. Kloß, A. Machalica, J. Kotschy, S. K. Vasa, P. A. Chater, C. Sternemann, M. T. Wharmby, R. Linser, R. Schmid, S. Henke, Frustrated flexibility in metal-organic frameworks. *Nat. Commun.* **12**, 4097 (2021).

4. J. E. Warren, C. G. Perkins, K. E. Jelfs, P. Boldrin, P. A. Chater, G. J. Miller, T. D. Manning, M. E. Briggs, K. C. Stylianou, J. B. Claridge, M. J. Rosseinsky, Shape selectivity by guest-driven restructuring of a porous material. *Angew. Chem. Int. Ed. Engl.* **53**, 4592–4596 (2014).

5. R. Matsuda, Selectivity from flexibility. *Nature* **509**, 434–435 (2014).

6. M. Eddaoudi, J. Kim, N. Rosi, D. Vodak, J. Wachter, M. O'Keeffe, O. M. Yaghi, Systematic design of pore size and functionality in isoreticular MOFs and their application in methane storage. *Science* **295**, 469–472 (2002).

7. H.-C. J. Zhou, S. Kitagawa, Metal-organic frameworks (MOFs). *Chem. Soc. Rev.* **43**, 5415–5418 (2014).

8. A. Schneemann, V. Bon, I. Schwedler, I. Senkovska, S. Kaskel, R. A. Fischer, Flexible metal-organic frameworks. *Chem. Soc. Rev.* **43**, 6062–6096 (2014).

9. V. N. Vukotic, K. J. Harris, K. Zhu, R. W. Schurko, S. J. Loeb, Metal-organic frameworks with dynamic interlocked components. *Nat. Chem.* **4**, 456–460 (2012).

10. T. Loiseau, C. Serre, C. Huguenard, G. Fink, F. Taulelle, M. Henry, T. Bataille, G. Férey, A rationale for the large breathing of the porous aluminum terephthalate (MIL-53) upon hydration. *Chemistry* **10**, 1373–1382 (2004).

11. C. Mellot-Draznieks, C. Serre, S. Surblé, N. Audebrand, G. Férey, Very large swelling in hybrid frameworks: A combined computational and powder diffraction study. *J. Am. Chem. Soc.* **127**, 16273–16278 (2005).

12. W. Meng, S. Kondo, T. Ito, K. Komatsu, J. Pirillo, Y. Hijikata, Y. Ikuhara, T. Aida, H. Sato, An elastic metal-organic crystal with a densely catenated backbone. *Nature* **598**, 298–303 (2021).

13. T. D. Bennett, A. K. Cheetham, A. H. Fuchs, F. X. Coudert, Interplay between defects, disorder and flexibility in metal-organic frameworks. *Nat. Chem.* **9**, 11–16 (2017).

14. A. B. Cairns, A. L. Goodwin, Structural disorder in molecular framework materials. *Chem. Soc. Rev.* **42**, 4881–4893 (2013).

15. T. D. Bennett, A. K. Cheetham, Amorphous metal-organic frameworks. *Acc. Chem. Res.* **47**, 1555–1562 (2014).

16. S. Ehrling, E. M. Reynolds, V. Bon, I. Senkovska, T. E. Gorelik, J. D. Evans, M. Rauche, M. Mendt, M. S. Weiss, A. Pöppl, E. Brunner, U. Kaiser, A. L. Goodwin, S. Kaskel, Adaptive response of a metal-organic framework through reversible disorder-disorder transitions. *Nat. Chem.* **13**, 568–574 (2021).

17. B. Bueken, F. Vermoortele, M. J. Cliffe, M. T. Wharmby, D. Foucher, J. Wieme, L. Vanduyfhuys, C. Martineau, N. Stock, F. Taulelle, V. Van Speybroeck, A. L. Goodwin, D. De Vos, A breathing zirconium metal-organic framework with reversible loss of crystallinity by correlated nanodomain formation. *Eur. J. Chem.* **22**, 3264–3267 (2016).

18. Y. Fu, Z. Kang, J. Yin, W. Cao, Y. Tu, Q. Wang, X. Kong, Duet of acetate and water at the defects of metal–organic frameworks. *Nano Lett.* **19**, 1618–1624 (2019).

19. K. Tan, H. Pandey, H. Wang, E. Velasco, K.-Y. Wang, H.-C. Zhou, J. Li, T. Thonhauser, Defect termination in the UiO-66 family of metal-organic frameworks: The role of water and modulator. *J. Am. Chem. Soc.* **143**, 6328–6332 (2021).

20. S. Krause, F. S. Reuter, S. Ehrling, V. Bon, I. Senkovska, S. Kaskel, E. Brunner, Impact of defects and crystal size on negative gas adsorption in DUT-49 analyzed by in situ ^{129}Xe NMR spectroscopy. *Chem. Mater.* **32**, 4641–4650 (2020).

21. T. M. McDonald, J. A. Mason, X. Kong, E. D. Bloch, D. Gygi, A. Dani, V. Crocellà, F. Giordanino, S. O. Odoh, W. S. Drisdell, B. Vlaisavljevich, A. L. Dzubak, R. Poloni, S. K. Schnell, N. Planas, K. Lee, T. Pascal, L. F. Wan, D. Prendergast, J. B. Neaton, B. Smit, J. B. Kortright, L. Gagliardi, S. Bordiga, J. A. Reimer, J. R. Long, Cooperative insertion of CO2 in diamine-appended metal-organic frameworks. *Nature* **519**, 303–308 (2015).

22. E. J. Kim, R. L. Siegelman, H. Z. H. Jiang, A. C. Forse, J. H. Lee, J. D. Martell, P. J. Milner, J. M. Falkowski, J. B. Neaton, J. A. Reimer, S. C. Weston, J. R. Long, Cooperative carbon capture and steam regeneration with tetraamine-appended metal-organic frameworks. *Science* **369**, 392–396 (2020).

23. A. C. Forse, M. I. Gonzalez, R. L. Siegelman, V. J. Witherspoon, S. Jawahery, R. Mercado, P. J. Milner, J. D. Martell, B. Smit, B. Blümich, J. R. Long, J. A. Reimer, Unexpected diffusion anisotropy of carbon dioxide in the metal-organic framework Zn$_2$(dobpdc). *J. Am. Chem. Soc.* **140**, 1663–1673 (2018).

24. S. R. Caskey, A. G. Wong-Foy, A. J. Matzger, Dramatic tuning of carbon dioxide uptake via metal substitution in a coordination polymer with cylindrical pores. *J. Am. Chem. Soc.* **130**, 10870–10871 (2008).

25. D. Britt, H. Furukawa, B. Wang, T. G. Glover, O. M. Yaghi, Highly efficient separation of carbon dioxide by a metal-organic framework replete with open metal sites. *Proc. Natl. Acad. Sci. U.S.A.* **106**, 20637–20640 (2009).

26. J. B. Lefton, K. Pekar, U. Haris, M. Zick, P. J. Milner, A. Lippert, L. Pejov, T. Runčevski, Defects formation and amorphization of Zn-MOF-74 crystals by post-synthetic interactions with bidentate adsorbates. *J. Mater. Chem. A. Mater.* **35**, 19698–19704 (2021).

27. J. Morales-Vidal, R. García-Muelas, M. A. Ortuño, Defects as catalytic sites for the oxygen evolution reaction in Earth-abundant MOF-74 revealed by DFT. *Cat. Sci. Technol.* **11**, 1443–1450 (2021).

28. D. Wu, W. Yan, H. Xu, E. Zhang, Q. Li, Defect engineering of Mn-based MOFs with rod-shaped building units by organic linker fragmentation. *Inorganica Chim. Acta.* **460**, 93–98 (2017).

29. B. Li, H. C. Zeng, Synthetic chemistry and multifunctionality of an amorphous Ni-MOF-74 shell on a Ni/SiO$_2$ hollow catalyst for efficient tandem reactions. *Chem. Mater.* **31**, 5320–5330 (2019).

30. P. Ma, F. Meng, N. Wang, J. Zhang, J. Xie, B. Dai, Heterogeneous amorphous Cu–MOF-74 catalyst for C-N coupling reaction. *ChemistrySelect* **3**, 10694–10700 (2018).

31. J. A. Villajos, N. Jagorel, S. Reinsch, F. Emmerling, Increasing exposed metal site accessibility in a Co-MOF-74 material with induced structure-defects. *Front. Mater.* **6**, 230 (2019).

32. L. Liu, Z. Chen, J. Wang, D. Zhang, Y. Zhu, S. Ling, K.-W. Huang, Y. Belmabkhout, K. Adil, Y. Zhang, B. Slater, M. Eddaoudi, Y. Han, Imaging defects and their evolution in a metal-organic framework at sub-unit-cell resolution. *Nat. Chem.* **11**, 622–628 (2019).

33. M. J. Cliffe, W. Wan, X. Zou, P. A. Chater, A. K. Kleppe, M. G. Tucker, H. Wilhelm, N. P. Funnell, F.-X. Coudert, A. L. Goodwin, Correlated defect nanoregions in a metal-organic framework. *Nat. Commun.* **5**, 4176 (2014).

34. C. A. Trickett, K. J. Gagnon, S. Lee, F. Gándara, H.-B. Bürgi, O. M. Yaghi, Definitive molecular level characterization of defects in UiO-66 crystals. *Angew. Chem. Int. Ed. Engl.* **54**, 11162–11167 (2015).

35. Y. Fu, H. Guan, J. Yin, X. Kong, Probing molecular motions in metal-organic frameworks with solid-state NMR. *Coord. Chem. Rev.* **427**, 213563 (2021).

36. A. J. Rossini, A. Zagdoun, M. Lelli, J. Canivet, S. Aguado, O. Ouari, P. Tordo, M. Rosay, W. E. Maas, C. Copéret, D. Farrusseng, L. Emsley, A. Lesage, Dynamic nuclear polarization enhanced solid-state NMR spectroscopy of functionalized metal-organic frameworks. *Angew. Chem. Int. Ed.* **51**, 123–127 (2012).

37. M. Hong, K. Schmidt-Rohr, Magic-angle-spinning NMR techniques for measuring long-range distances in biological macromolecules. *Acc. Chem. Res.* **46**, 2154–2163 (2013).

38. K. Schmidt-Rohr, H. W. Spiess, in *Multidimensional Solid-State NMR and Polymers* (Academic Press, 1994), p. 478.

39. A. Sutrisno, Y. Huang, Solid-state NMR: A powerful tool for characterization of metal-organic frameworks. *Solid State Nucl. Magn. Reson.* **49–50**, 1–11 (2013).

40. S. E. Ashbrook, D. M. Dawson, V. R. Seymour, Recent developments in solid-state NMR spectroscopy of crystalline microporous materials. *Phys. Chem. Chem. Phys.* **16**, 8223–8242 (2014).

41. X. Kong, H. Deng, F. Yan, J. Kim, J. A. Swisher, B. Smit, O. M. Yaghi, J. A. Reimer, Mapping of functional groups in metal-organic frameworks. *Science* **341**, 882–885 (2013).

42. Z. Pang, J. Zhang, W. Cao, X. Kong, X. Peng, Partitioning surface ligands on nanocrystals for maximal solubility. *Nat. Commun.* **10**, 2454 (2019).

43. T. M. McDonald, W. R. Lee, J. A. Mason, B. M. Wiers, C. S. Hong, J. R. Long, Capture of carbon dioxide from air and flue gas in the alkylamine-appended metal-organic framework mmen-Mg$_2$(dobpdc). *J. Am. Chem. Soc.* **134**, 7056–7065 (2012).

44. J. B. Decoste, G. W. Peterson, Metal-organic frameworks for air purification of toxic chemicals. *Chem. Rev.* **114**, 5695–5727 (2014).

45. F. Jeremias, D. Fröhlich, C. Janiak, S. K. Henninger, Water and methanol adsorption on MOFs for cycling heat transformation processes. *New J. Chem.* **38**, 1846–1852 (2014).

46. T. Gullion, J. Schaefer, Development of REDOR rotational-echo double-resonance NMR. *J. Magn. Reson.* **81**, 196–200 (1989).

47. W. Luo, M. Hong, Determination of the oligomeric number and intermolecular distances of membrane protein assemblies by anisotropic 1H-driven spin diffusion NMR spectroscopy. *J. Am. Chem. Soc.* **128**, 7242–7251 (2006).

48. E. R. DeAzevedo, W.-G. Hu, T. J. Bonagamba, K. Schmidt-Rohr, Centerband-only detection of exchange: Efficient analysis of dynamics in solids by NMR. *J. Am. Chem. Soc.* **121**, 8411–8412 (1999).

49. M. Bertmer, H. Eckert, Dephasing of spin echoes by multiple heteronuclear dipolar interactions in rotational echo double resonance NMR experiments. *Solid State Nucl. Magn. Reson.* **15**, 139–152 (1999).

50. A. F. Sapnik, I. Bechis, S. M. Collins, D. N. Johnstone, G. Divitini, A. J. Smith, P. A. Chater, M. A. Addicoat, T. Johnson, D. A. Keen, K. E. Jelfs, T. D. Bennett, Mixed hierarchical local structure in a disordered metal-organic framework. *Nat. Commun.* **12**, 2062 (2021).

51. J. Fonseca, T. Gong, L. Jiao, H.-L. Jiang, Metal–organic frameworks (MOFs) beyond crystallinity: Amorphous MOFs, MOF liquids and MOF glasses. *J. Mater. Chem. A.* **9**, 10562–10611 (2021).

52. M. J. Frisch, G. W. Trucks, H. B. Schlegel, G. E. Scuseria, M. A. Robb, J. R. Cheeseman, G. Scalmani, V. Barone, B. Mennucci, G. A. Petersson, H. Nakatsuji, M. Caricato, X. Li, H. P. Hratchian, A. F. Izmaylov, J. Bloino, G. Zheng, J. L. Sonnenberg, M. Hada, M. Ehara, K. Toyota, R. Fukuda, J. Hasegawa, M. Ishida, T. Nakajima, Y. Honda, O. Kitao, H. Nakai, T. Vreven, J. A. Montgomery, Jr., J. E. Peralta, F. Ogliaro, M. Bearpark, J. J. Heyd, E. Brothers, K. N. Kudin, V. N. Staroverov, R. Kobayashi, J. Normand, K. Raghavachari, A. Rendell, J. C. Burant, S. S. Iyengar, J. Tomasi, M. Cossi, N. Rega, J. M. Millam, M. Klene, J. E. Knox, J. B. Cross, V. Bakken, C. Adamo, J. Jaramillo, R. Gomperts, R. E. Stratmann, O. Yazyev, A. J. Austin, R. Cammi, C. Pomelli, J. W. Ochterski, R. L. Martin, K. Morokuma, V. G. Zakrzewski, G. A. Voth, P. Salvador, J. J. Dannenberg, S. Dapprich, A. D. Daniels, O. Farkas, J. B. Foresman, J. V. Ortiz, J. Cioslowski, D. J. Fox, in *Gaussian 09, Revision E.01* (Gaussian Inc., 2013).

53. J. Wang, R. M. Wolf, J. W. Caldwell, P. A. Kollman, D. A. Case, Development and testing of a general amber force field. *J. Comput. Chem.* **25**, 1157–1174 (2004).

54. J. Wang, W. Wang, P. A. Kollman, D. A. Case, Automatic atom type and bond type perception in molecular mechanical calculations. *J. Mol. Graph. Model.* **25**, 247–260 (2006).

55. M. J. Abraham, T. Murtola, R. Schulz, S. Páll, J. C. Smith, B. Hess, E. Lindah, Gromacs: High performance molecular simulations through multi-level parallelism from laptops to supercomputers. *SoftwareX* **1–2**, 19–25 (2015).

56. S. Pronk, S. Páll, R. Schulz, P. Larsson, P. Bjelkmar, R. Apostolov, M. R. Shirts, J. C. Smith, P. M. Kasson, D. Van Der Spoel, B. Hess, E. Lindahl, GROMACS 4.5: A high-throughput and highly parallel open source molecular simulation toolkit. *Bioinformatics* **29**, 845–854 (2013).

57. D. Van Der Spoel, E. Lindahl, B. Hess, G. Groenhof, A. E. Mark, H. J. C. Berendsen, GROMACS: Fast, flexible, and free. *J. Comput. Chem.* **26**, 1701–1718 (2005).

58. L. Martinez, R. Andrade, E. G. Birgin, J. M. Martinez, PACKMOL: A package for building initial configurations for molecular dynamics simulations. *J. Comput. Chem.* **30**, 2157–2164 (2009).

59. D. J. Evans, B. L. Holian, The nose-hoover thermostat. *J. Chem. Phys.* **83**, 4069–4074 (1985).

60. B. Hess, H. Bekker, H. J. C. Berendsen, J. G. E. M. Fraaije, LINCS: A linear constraint solver for molecular simulations. *J. Comput. Chem.* **18**, 1463–1472 (1997).

61. T. Darden, D. York, L. Pedersen, Particle mesh Ewald: An $N \cdot \log(N)$ method for Ewald sums in large systems. *J. Chem. Phys.* **98**, 10089–10092 (1993).

62. W. Humphrey, A. Dalke, K. Schulten, VMD: Visual molecular dynamics. *J. Mol. Graph.* **14**, 33–38 (1996).

63. A. A. Coelho, Topas Academic: General profile and structure analysis software for powder diffraction data (Bruker AXS, 2007).

64. G. S. Pawley, Unit-cell refinement from powder diffraction scans. *J. Appl. Cryst.* **14**, 357–361 (1981).

65. K. Schmidt-Rohr, H. W. Spiess, in *Multidimensional Solid-State NMR and Polymers* (Academic Press, 1994), p. 478.